



Evaluation of static recrystallization and grain growth kinetics of hot-rolled AZ31 alloy

Salaheddine SADI¹, Abdelkader HANNA¹, Thierry BAUDIN², Anne-Laure HELBERT², François BRISSET², Djamel BRADAI³, and Hiba AZZEDDINE^{1,*}

¹ Laboratory of Materials and Renewable Energy, Faculty of Sciences, Mohamed Boudiaf University, 28000, M'sila, Algeria

² Université Paris-Saclay, CNRS, Institut de chimie moléculaire et des matériaux d'Orsay, 91405, Orsay, France

³ Laboratory of Materials Physics, Faculty of Physics, University of Sciences and Technology - Houari Boumediene (USTHB), Bab-Ezzouar, 16111, Algiers, Algeria

*Corresponding author e-mail: hiba.azzeddine@univ-msila.dz

Received date:

17 September 2021

Revised date:

6 November 2021

Accepted date:

22 November 2021

Keywords:

Activation energy;
AZ31 alloy;
Grain growth;
Kinetics;
Static recrystallization

Abstract

The static recrystallization/grain growth kinetics of the AZ31 (Mg-3Al-1Zn, wt%) alloy were investigated employing Vickers microhardness and electron backscatter diffraction (EBSD) measurements. The AZ31 alloy was subject to a hot-rolling for 70% of thickness reduction and then annealed at various temperatures (150°C, 250°C, and 350°C) from 5 min to 24 h. First, the static recrystallization kinetics were analysed by means of the Johnson-Mehl-Avrami-Kolmogorov (JMAK) model. The results showed that the recrystallization occurred under two regimes both involving their own Avrami exponent/activation energy. In regime I, the Avrami exponent was found in the range of 1.5-0.35 depending on the annealing temperature and activation energy of 74.1 ± 5.7 kJ·mol⁻¹. In regime II, an identical value of Avrami exponent was found (0.1-0.2) and a very low activation energy of 14.8 ± 0.7 kJ·mol⁻¹ was found for all annealing conditions. Non-random nucleation sites such as shear bands were considered as the main factor responsible for the deviation from the JMAK model. Moreover, the grain growth kinetics was well fitted by the general $D^m - D_0^m = ct$ equation where $c = c_0 \exp\left(-\frac{Q_g}{RT}\right)$. Accordingly, $Q_g = 109 \pm 0.2$ kJ·mol⁻¹ which is median between grain boundary diffusion and bulk diffusion values for Mg and its alloys. The derived activation energies were discussed in terms of influencing factors such as solute drag, formation of basal texture, and microstructural heterogeneities like shear bands and twinning.

1. Introduction

Nowadays, transportation industries are more interested on lightweight design to reach rigorous necessities of fuel productivity and reduce environmental pollution. Lightweight magnesium (Mg) based alloys are promising candidates for these industries owing to their excellent strength-to-weight ratio [1,2]. Nevertheless, at low deformation temperatures, Mg-based alloys endure poor formability because of a lack of deformation mechanisms and the development of sharp basal texture during deformation processing which border their potential structural applications [3].

Microstructural changes, which mainly are grain refinement and texture weakening through dynamic recrystallization (DRX) and/or static recrystallization (SRX) during thermomechanical processing are the keys to the development of a new class of Mg-based alloys with required properties [4-8]. At high temperatures, the formability of Mg-based alloys is increased and improved since further slip systems could be thermally activated and also due to the occurrence of DRX. In fact, DRX is the principal mechanism responsible for grain refinement in Mg-based alloys during deformation processing [9-16].

The Hall-Petch relationship indicates that the strength of a material increases through decreasing the grain size and incidentally because

to the increase of the number of grain boundaries that prevent the dislocation motion [17]. However, grain growth generally occurs during the SRX process and causes the loss of thermal stability [18-23]. Consequently, it is crucial to distinguish the static recrystallization/grain growth kinetics of Mg-based alloys.

Usually, any assessment of the static recrystallization/grain growth kinetics is based on two parameters: 1) a phenomenological exponent which characterizes the mechanism responsible for recrystallization and/or the grain growth and 2) the activation energy which determines the magnitude of the resistance to any grain growth. For Mg-based alloys, the calculated activation energies for recrystallization/grain growth are generally compared with grain boundary diffusion activation energy (92 kJ·mol⁻¹) or with the lattice self-diffusion energy (135 kJ·mol⁻¹) [24]. However, a deviation from these values due to the presence of inhomogeneous nucleation sites such as twinning and shear bands formed during deformation processing is often reported [9,12,18,19, 21,25-28]. Besides, the static recrystallization/grain growth kinetics of Mg-based alloys are strongly related to their metallurgical and microstructural states and parameters such as alloying elements, grain size, grains orientation, nature and geometry of grain boundaries, and the distribution of particles [29-33].

In addition to the importance of annealing conditions, i.e., temperature and duration, deformation processing conditions including strain rate, deformation temperature, and thickness reduction in the case of rolling process do greatly affect the static recrystallization/grain growth kinetics. For example, it was expected that the static recrystallization rate might increase with increasing thickness reduction because of the increase of the stored energy at higher thickness reduction [26]. However, this is true only when the DRX did not occur during deformation processing [21]. Moreover, the absence of DRX led to the weakening of texture during subsequent annealing [34, 35]. Otherwise, the deformation texture is retained during annealing [20]. As a new insight, the severe plastic deformation (SPD) resulted in more complicated grain growth kinetics resulting from the large amounts of extrinsic dislocations and the competition of occurrence of SRX during the SPD processing [23,36,37]. The presence of two ranges of grain growth activation energy depending on the annealing temperature was described in severely deformed Mg-1.43Nd (wt%) and AZ31 (Mg-3Al-1Zn, wt%) alloys [23,36].

There has been substantial work, particularly in the last 10 years, and with it significant improvements in our understanding of the recrystallization/grain growth behaviour in Mg-based alloys. However, much work is still needed to well understand the static recrystallization/grain growth kinetics and to have valuable data on the deformation and annealing treatments for the optimization and control of the physical and metallurgical properties of forthcoming designed Mg-based alloys.

In this frame, the goal of this work is an investigation of the role of annealing temperature and duration on the static recrystallization/grain growth kinetics of hot-rolled AZ31 alloy. First, the alloy was hot-rolled at 350°C to 70% of thickness reduction and then annealed at various temperatures (150°C, 250°C, and 350°C) from 5 min to 24 h. This work is a part of a series of investigations on the AZ31 alloy regarding the effect of rolling conditions and annealing treatments on corrosion behaviour [34,38]. So far, the results confirmed that small grain size combined with weak texture greatly enhanced the corrosion behavior of the AZ31 alloy [34,38]. It is believed that the present work will help to provide more data to ameliorate the design of AZ31 alloy.

2. Experimental procedures

The sheet AZ31 alloy was generously given from MagIC (Magnesium Innovations Center), Germany.

The AZ31 alloy was subject to hot-rolling at 350°C for 70 % of thickness reduction with 10% of thickness reduction (0.22 mm/pass) in each pass to avoid any sample cracking. Then, the deformed samples were annealed at 150°C, 250°C, and 350°C for times ranging from 5 min to 24 h.

The mean grain size of the different samples was estimated by optical microscopy the line intercept method. For that, the samples were metallographically prepared by mechanical grinding and electropolishing with 5 parts of ethanol and 3 parts of phosphoric acid for 30 min and then etched at room temperature for 3 s in a solution containing 5% HNO₃, 15% acetic acid, 60% ethanol, and 20% distilled water. At least four fields were exploited for an accurate mean grain size measurement and evaluating the grain growth kinetics.

EBSD measurements were performed using a FEG-SEM SUPRA 55 VP field emission gun scanning electron microscope working at 20 kV in the mid-thickness of the RD-ND plane of the samples (RD and ND mean the rolling and normal directions, respectively). A standard clean-up procedure was used to analyze the orientation imaging microscopy (OIM) data [11,12,23,39]. The scanned areas were 400 μm² × 400 μm² with a 1 μm step size for deformed and annealed samples at 250°C and 350°C, respectively and were 200 μm² × 200 μm² with a 1 μm step size for annealed samples at 150°C. In addition, smaller areas of 100 μm² × 100 μm² and a step size of 0.5 μm were scanned to examine twins and shear bands. The analysis of the crystallographic texture from EBSD measurements was performed using MText software [40].

Vickers microhardness of the samples was measured with a load of 100 g (Hv_{0.1}) and a 10 s of a holding time.

3. Results and discussion

3.1 Deformation microstructure

Figure 1 reveals the OIM in inverse pole figure (TD-IPF, TD is the transverse direction), image quality (IQ) superposed with grain boundaries and grain orientation spread (GOS) maps of the deformed AZ31 alloy, respectively. The grain boundaries were divided as sub-grains boundaries (SGBs) with misorientation $\theta < 2^\circ$, low angle boundaries (LAGBs) with $2^\circ < \theta < 5^\circ$, medium angle grain boundaries (MAGBs) with $5^\circ < \theta < 15^\circ$, and high angle boundaries (HAGBs) with $\theta > 15^\circ$, respectively.

GOS approach allows quantifying the fraction of recrystallized grains, F_{rex} , by assuming a deviation from the average orientation of the recrystallized grains less than 2° [15,41]. The F_{rex} is shown on the upper side of the GOS map.

The TD-IPF map shows that the microstructure is formed of equiaxed grains with a value of $9.2 \pm 1.2 \mu\text{m}$ in which several twins are present as indicated by arrows. However, the IQ map demonstrates the heterogeneity of the deformed microstructure by the formation of shear bands tilted about 30° to 36° from RD. In Mg-based alloys, the shear bands are formed due to the activation of twinning [42] or the occurrence of DRX along the grain boundaries [43]. The GOS map shows that only 10% of grains were dynamically recrystallized during hot-rolling and no evidence of the formation of recrystallized grains on the grain boundaries. While twinning, including: extension twins ($86^\circ < 11\bar{2}0 >$ in green), contraction twins ($56^\circ < 11\bar{2}0 >$ in red), double twins ($38^\circ < 11\bar{2}0 >$ in blue) and $22^\circ < 11\bar{2}0 >$ (in yellow), is noticed inside the shear band as zoomed in Figure 1(d) (yellow box in Figure 1(b)). The present result may suggest that the shear bands were formed due to the activation of twinning. High fraction of LAGBs can be seen inside the shear bands (Figure 1(b)) indicating the formation of sub-grains which further will transform to new recrystallized grains during subsequent annealing.

3.2 Static recrystallization kinetics

Figure 2 displays the evolutions of microhardness versus the annealing time of the annealed AZ31 alloy at 150°C, 250°C and 350°C. The microhardness value of the deformed sample is $73.0 \pm 1.2 \text{ Hv}$

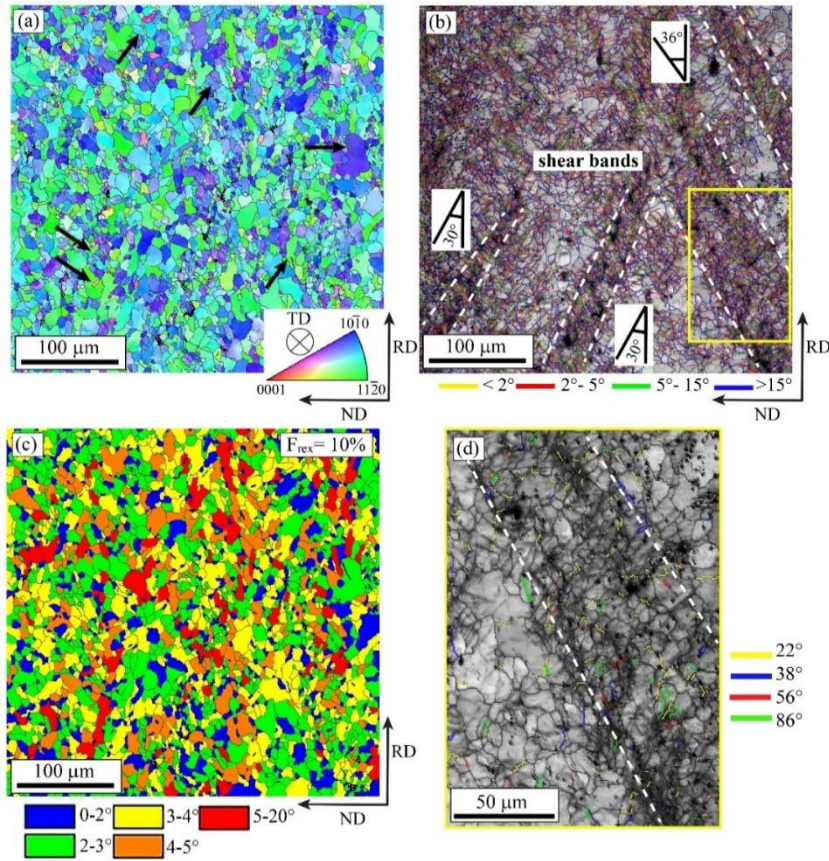


Figure 1. (a) TD-IPF, (b) IQ, (c) GOS maps display the microstructure of the deformed AZ31 alloy, and (d) IQ map highlighted with different twin types of the zoomed area indicated in Figure 1(b) (yellow box)

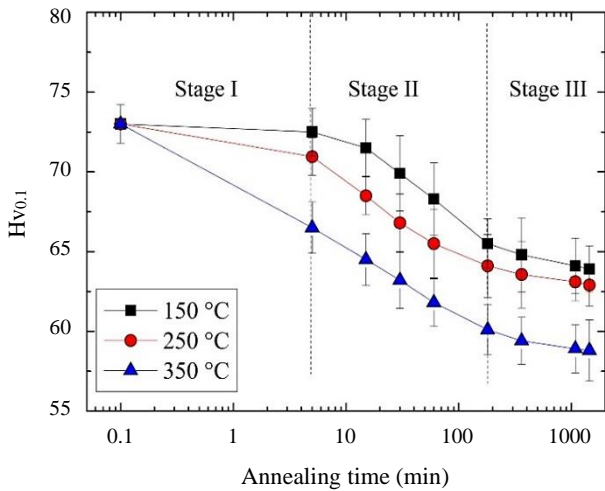


Figure 2. Microhardness evolution of annealed AZ31 alloy versus the annealing time at 150°C, 250°C, and 350°C.

The microhardness decreases with the increase of annealing time and can be separated into 3 stages: stage I observed only in samples annealing at 150°C and 250°C where the microhardness did not change with annealing time (72.5±1.5 Hv and 70.9±1.1 Hv after 5 min of annealing at 150°C and 250°C, respectively) indicating a recovery process. Stage II where the microhardness decreases continuously with annealing time owing to the recrystallization process. In stage III, the microhardness more-or-less decreases with a further increase

of annealing time indicating the completion of the recrystallization process. The microhardness reached values of 63.9±1.4 Hv, 62.9±1.3 Hv and 58.8±1.9 Hv after annealing for 24 h at 150°C, 250°C and 350°C, respectively.

Quantitatively, the isothermal static recrystallization kinetics is defined according to the Johnson–Mehl–Avrami–Kolmogorov (JMAK) model [44]

$$X = 1 - \exp(-kt^n) \tag{1}$$

where X is the recrystallized fraction, k a temperature-dependent constant, and n the Avrami exponent. According to the JMAK equation, the values of n and k are strongly linked to the nature of grain nucleation and grain growth. Table 1 presents the ideal values of the n exponent [45]. The temperature-dependent constant k , can be stated as:

$$k = k_0 \exp\left(-\frac{Q}{RT}\right) \tag{2}$$

where k_0 is a constant, Q the activation energy for the recrystallization, $R = 8.314 \text{ J}\cdot\text{mol}^{-1}\cdot\text{K}^{-1}$ the gas constant and T the annealing temperature.

To obtain the n and k values, it is required to rescript the Equation (1) as:

$$\ln\left(\ln\left(\frac{1}{1-X}\right)\right) = \ln k + n \ln t \tag{3}$$

Table 1. Ideal values for Avrami exponent, n depending on the nature of nucleation/growth of grains [45].

Growth geometry	Site saturation	Constant nucleation rate
Three dimensions	3	4
Two dimensions	2	3
One dimension	1	2

Consequently, n is the slope of the $\ln \left(\ln \left(\frac{1}{1-X} \right) \right)$ versus $\ln(t)$ plot and $\ln(k)$ is the y-intercept.

The recrystallized fraction, X can be calculated using the microhardness values following the equation:

$$X = \frac{Hv_{def} - Hv_t}{Hv_{def} - Hv_f} \quad (4)$$

where Hv_{def} , Hv_t and Hv_f stand for the microhardness of the deformed, annealed sample at time t and after complete recrystallization, respectively. The Hv_f value was chosen as for the sample annealed for 24 h at 350°C since the GOS maps shown in Figure 3 demonstrated that in this condition the alloy exhibits a high recrystallization fraction (93% with GOS > 2°) compared to those annealed at 150°C and 250°C for the same time (24 h), i.e., 48 and 67%, respectively.

In addition, about 10% of the deformed microstructure was

dynamically recrystallized (Figure 1), hence the real fraction of static recrystallization can be estimated using the following equation:

$$X_{real} = (1 - X_0)X - X_0 \quad (5)$$

where X_0 is the fraction of dynamically recrystallized grains.

Figure 4(a) shows the $\ln \left(\ln \left(\frac{1}{1-X} \right) \right)$ against $\ln(t)$ for the annealed AZ31 alloy. As can be noticed, the experimental data were lie in two straight lines for each temperature indicating the production of two regimes with their own values of n and k . The two regimes coincide with the stage II and III observed in the evolution of micro-hardness against the annealing time (Figure 2). Table 2 summarizes the values of n and $\ln(k)$ for both regimes in the different samples. In addition, the activation energy of regimes I and II can be calculated by plotting $\ln(k)$ against $1000/RT$ as presented in Figure 4(b) and their values are also consigned in Table 2.

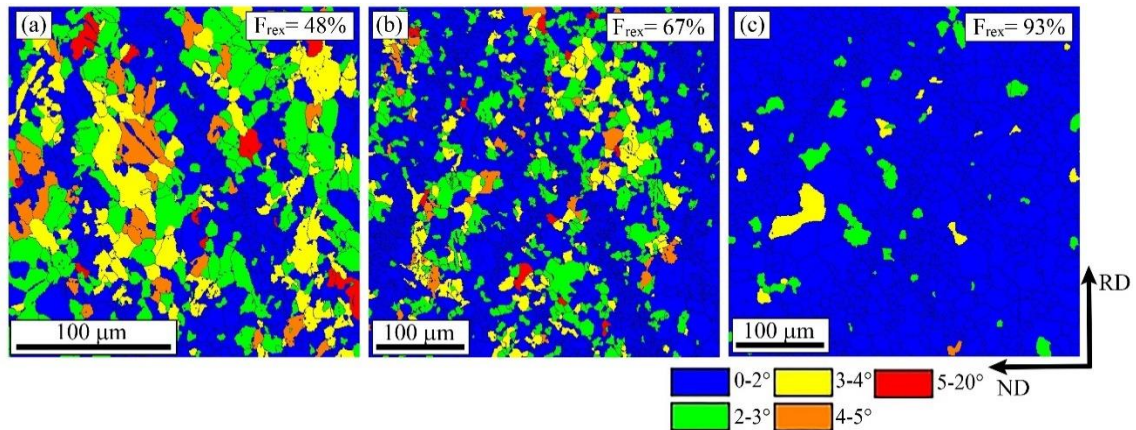


Figure 3. GOS maps of annealed AZ31 alloy for 24 h at: (a) 150°C, (b) 250°C, and (c) 350°C. The fraction of recrystallization is shown in the upper of the maps.

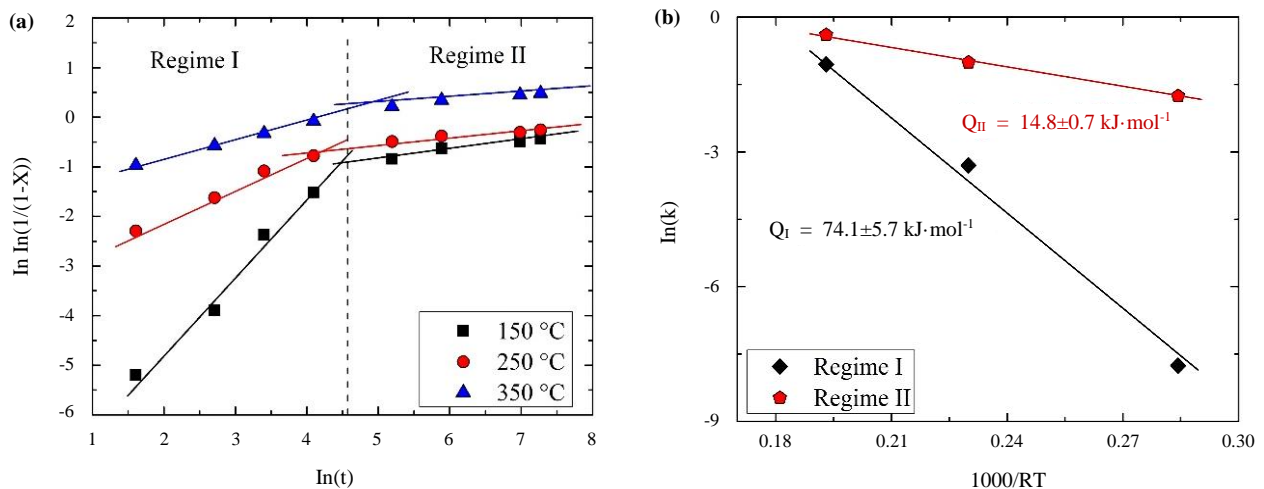


Figure 4. (a) $\ln \left(\ln \left(\frac{1}{1-X} \right) \right)$ against $\ln(t)$ and (b) $\ln(k)$ as a function of $1000/RT$ for the annealed AZ31 alloy at 150°C, 250°C, and 350°C, respectively.

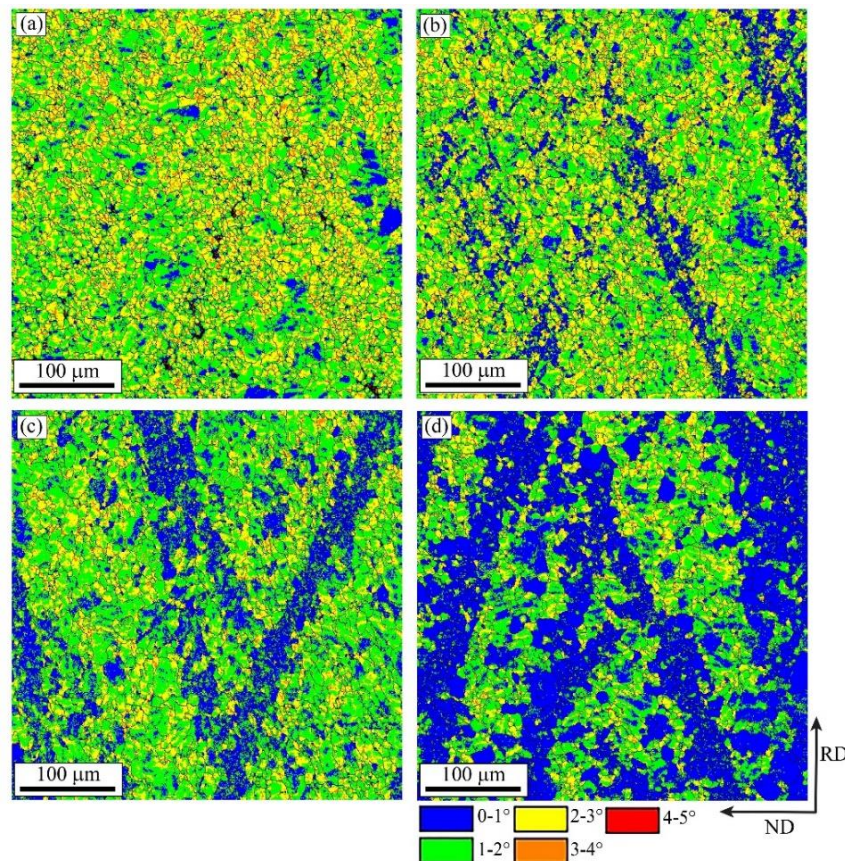
Table 2. Values of Avrami exponent n , and activation energy Q , in different regimes found for the present alloy.

Annealing Temperature	Regime I			Regime II		
	n	$\ln(k)$	Q_I (kJ·mol ⁻¹)	n	$\ln(k)$	Q_{II} (kJ·mol ⁻¹)
150 °C	1.52 ±0.13	-7.76 ±0.41	74.1±5.7	0.18 ±0.02	-1.76±0.17	14.8±0.7
250 °C	0.62 ±0.03	-2.30±0.11		0.10 ±0.01	-1.01±0.08	
350 °C	0.35 ±0.02	-1.05 ±0.01		0.12 ±0.01	-0.40±0.08	

The Avrami exponent of regime I decreases with increasing annealing temperature from $n_I = 1.52$ at 150°C to $n_I = 0.62$ at 250°C and then to $n_I = 0.35$ at 350°C indicating a strong dependency of the recrystallization mechanisms on the annealing temperature. While for regime II the n_2 values in the three annealing conditions were very similar around 0.1-0.2 and relatively lower than those for regime I. Based on Table 1, the growth geometry of the recrystallized grains can be presumed to be 1 dimension. The presence of two regimes in the three annealing temperature conditions demonstrated that the static recrystallization kinetics is strongly related to the deformation microstructure. The fitting of the JMAK model into two regimes with two Avrami exponents is rarely reported for Mg-Al alloys [21, 25] but it has been reported for different deformed metals such as oxygen-free high conducting (OFHC) copper [46], low carbon steel [47] and iron [48]. This two-regime behavior was explained by the heterogeneity of nucleation of recrystallized grains [47]. Apparently, during the first regime, the region with high stored energy will be rapidly expanded by the recrystallization nuclei. Subsequently, the remained deformed region with lower stored energy will be progressively recrystallized and this corresponds to the second regime [47].

Kernel average misorientation (KAM) method allows the quantification of dislocation density (i.e., the stored energy) generated from geometrically necessary dislocations [49,50]. Figure 5 presents the KAM maps of the deformed and annealed AZ31 at 250°C, respectively. As shown, the grains formed in the shear bands have the lowest stored energy i.e lower dislocation density (blue color) compared with the other regions which means that the recrystallization took place first at the shear bands and then with progressively increasing annealing time at the rest of the microstructure.

Globally, the n values obtained from the present investigation are lower than the ideal values (Table 1), except for the sample annealed at the lowest temperature of 150°C. Many experimental studies on various metals reported the deviation of Avrami exponent from the theoretical values [9,12,18,19,21,26-28,51-54]. For example, the Avrami exponent was found in the range of 0.27-3.4 for AZ31 alloy under different deformation and annealing conditions [9,18,19,21,26-28,51]. Moreover, a lower n range (0.6-0.9) was also reported in processed and annealed Mg-RE alloys [12,51].

**Figure 5.** KAM maps of the AZ31 alloy: (a) deformed and annealed at 250°C for (b) 5 min, (c) 30 min, and (d) 24 h.

Two major reasons were anticipated to explain the low n values [33]. The first reason is the non-random recrystallization sites existing in the processed material. The second reason is being the growth rate of the nuclei which is not constant during the recrystallization process [33]. As can be seen, the deformed microstructure shown in Figure 1 clearly demonstrated the presence of large zones of shear bands and many twins. It is well known that these deformation features are perfect sites for the formation of new recrystallized grains which will conduct to a non-random distribution of nuclei and result in different growth rates. In addition, Figure 6 clearly shows that the microstructure is heterogeneous even after annealing for 24 h. All samples exhibit a bimodal grain size distribution where the small grains are mostly located in the shear bands as indicated by the delineated areas in Figure 6. It can be observed that the microstructures of the samples annealed for 5 min at 150°C and 250°C contain twinning (see arrows). The recrystallization of the samples annealed for 5 min at 150°C is delayed compared to the samples annealed at 250°C and 350°C at the same time. The creation of recrystallized grains is more visible in samples annealed at 250°C and 350°C for 5 min. This is attributed to the relatively higher temperature that results in a higher rate of nucleation and growth and enhanced kinetics which explain the decrease of Avrami exponent n_1 with increasing annealing

temperature. Apparently, the dependence of recrystallization kinetics on the annealing temperature is observed only during the first regime since the Avrami exponent of the second regime n_2 was found similar in the three annealing conditions. This indicates that most of the recrystallization process occurred during the first regime.

The activation energy of regime I is equal to $74.1 \pm 5.7 \text{ kJ}\cdot\text{mol}^{-1}$ which is lower than the boundary self-diffusion energy ($92 \text{ kJ}\cdot\text{mol}^{-1}$) and the lattice self-diffusion energy ($135 \text{ kJ}\cdot\text{mol}^{-1}$) [24]. Low activation energy of $85.9 \text{ kJ}\cdot\text{mol}^{-1}$ was also reported in heavily cold-drawn and annealed AZ31 alloy [19] and in the range of $65 \text{ kJ}\cdot\text{mol}^{-1}$ to $88 \text{ kJ}\cdot\text{mol}^{-1}$ depending on the thickness of the twin-roll casting AZ31 alloy [26]. The reduced activation energy found in the various AZ31 alloys is mostly attributed to the acceleration of static recrystallization due to the occurrence of heterogeneities such as shear bands. The amount of the activation energy of regime II was found very small $\sim 14.8 \pm 0.7 \text{ kJ}\cdot\text{mol}^{-1}$ compared to regime I. It can be speculated that at this stage the completion of the recrystallization process did not require high activation energy. This can be confirmed by the slow decrease of the microhardness value (stage III) shown in Figure 2 indicating that the recrystallized fraction remained almost the same at this stage.

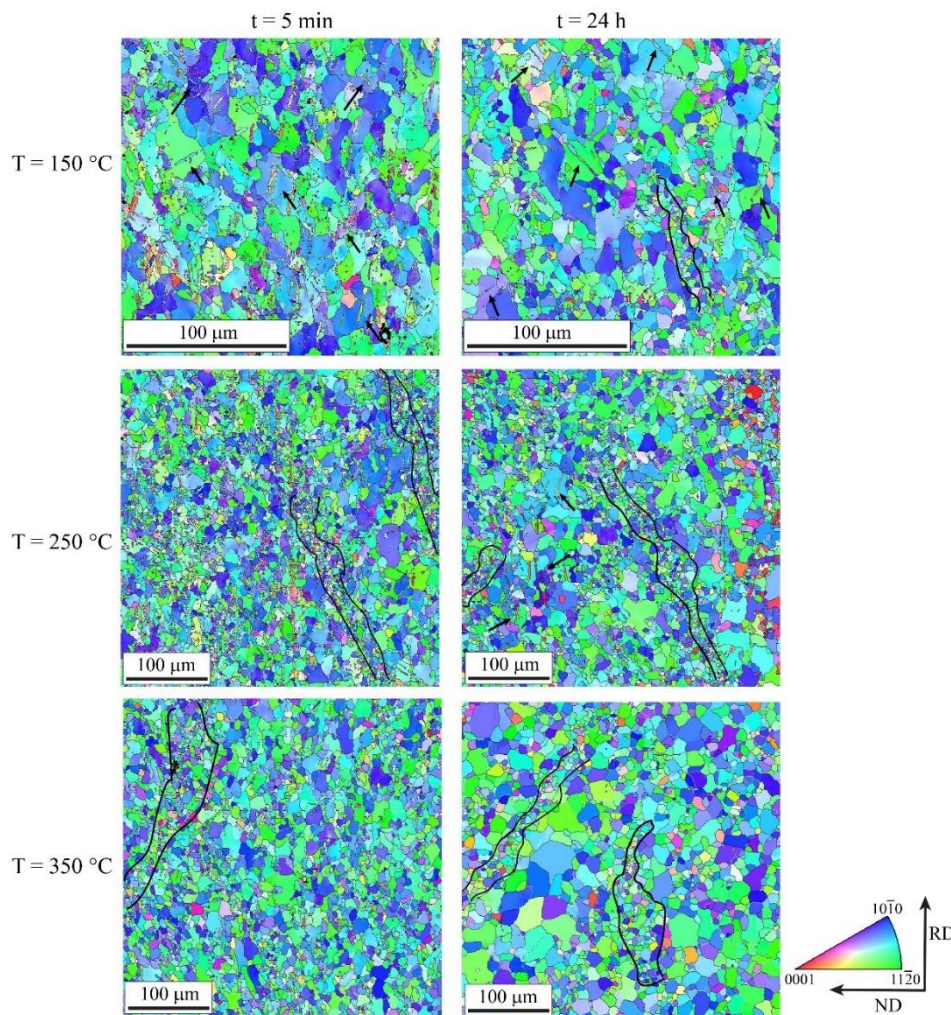


Figure 6. TD-IPF maps showing the evolution of microstructure of the AZ31 alloy annealed at 150°C, 250°C and 350°C for 5 min and 24 h, respectively. A bimodal grain size distribution is evidenced. Arrows show twinning.

Table 3. Fitting parameters of the recrystallized fraction X with the modified JMAK equation.

Annealing Temperature	Regime I			Regime II	
	A	n_1	$\ln(k_1)$	n_2	$\ln(k_2)$
150 °C	0.35	1.5	-6.50	0.7	-7.09
250 °C	0.40	0.8	-5.25	0.4	-5.38
350 °C	0.35	0.4	-3.47	0.5	-1.51

A modified JMAK equation that involves two Avrami exponents was proposed as follow [55]:

$$X = A\{1 - \exp(-k_1 t^{n_1})\} + (1-A)\{1 - \exp(-k_2 t^{n_2})\} \quad (6)$$

Where A is the fraction of recrystallization in the first regime.

The results of the recrystallized fraction fitted with the modified JMAK equation are presented in Figure 7 and the fitting parameters are shown in Table 3.

The fitted curves using the two Avrami exponents equation fit well with the experimental ones, especially for the first regime. It seems that the second regime started when 35% to 40% (corresponding to A values) of the microstructure have been recrystallized.

3.3 Grain growth kinetics

The plot of the mean grain size versus the annealing time of the annealed AZ31 alloy is shown in Figure 8. As expected, the grain size increases with increasing annealing conditions (temperature and duration). The grain size of the as deformed sample ($9.2 \pm 1.2 \mu\text{m}$) increases to about $15.1 \pm 1.3 \mu\text{m}$, $18.2 \pm 1.2 \mu\text{m}$, and $21.2 \pm 1.0 \mu\text{m}$ after 24 h annealing at 150°C, 250°C and 350°C, respectively. It is noticeable that for all annealing temperature conditions the grain size increases rapidly up to 180 min and then the grain growth rate becomes slow during a longer duration.

The grain growth kinetics is investigated following the general equation [56]:

$$D^m - D_0^m = ct \quad (7)$$

Where D is the mean grain size at the annealing time t , D_0 is the initial mean grain size at $t = 0$ (the deformed state), m is the grain growth exponent and c is a grain growth rate constant and can follow the Arrhenius equation:

$$c = c_0 \exp\left(-\frac{Q_g}{RT}\right) \quad (8)$$

where c_0 is a pre-exponential constant and Q_g the activation energy of grain growth.

The rate of the grain growth process, dD/dt , can be resulted from Equation (6):

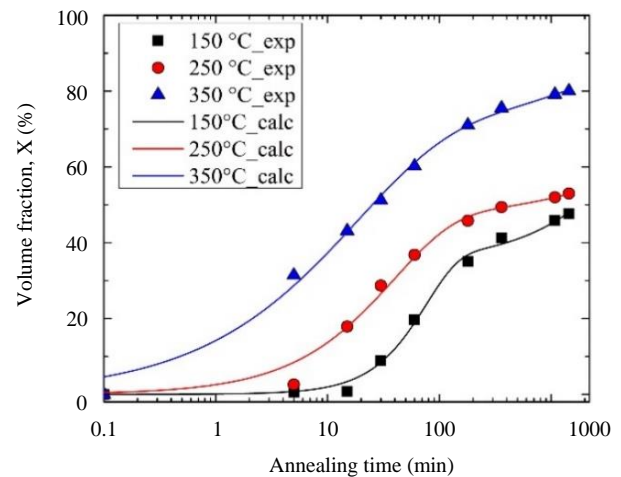
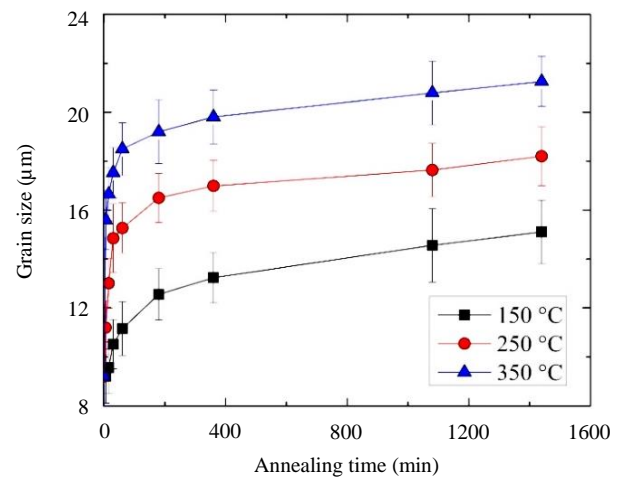
$$\ln\left(\frac{dD}{dt}\right) = (1-m)\ln D + \ln\left(\frac{c}{m}\right) \quad (9)$$

The slope of the curve $\ln(dD/dt)$ against $\ln(D)$ allowed the determination of grain growth exponent m . The m assumed that the migrating boundary rate is relative to the driving pressure on that boundary [18]. Ideally in the case of defect-free metals $m = 2$. This

assumed parabolic growth law and it is expected to hold for both two and three-dimension microstructures [56].

Figure 9(a) presents the evolution of $\ln(dD/dt)$ against $\ln(D)$ for the annealed AZ31 alloy at different annealing temperatures. The grain growth exponent m was equal to 7.9, 9.5, and 10.3 at 150°C, 250°C, and 350°C, respectively. The m value was found in the range of 2 to 15 in Mg-based alloys under various deformation and recrystallization conditions [18,20,30,57-63].

The activation energy can be evaluated by plotting $\ln c$ as a function of $1000/RT$ as shown in Figure 9(b). The activation energy was found equal to $109.2 \pm 0.2 \text{ kJ}\cdot\text{mol}^{-1}$. It is slightly higher (+15%) than found for grain boundary diffusion in Mg ($92 \text{ kJ}\cdot\text{mol}^{-1}$) and lower (-24%) than reported for bulk diffusion in Mg ($135 \text{ kJ}\cdot\text{mol}^{-1}$). It can be considered that the activation energy of the present alloy is intermediate to the grain boundary diffusion and bulk diffusion in Mg values.

**Figure 7.** Fitting of the recrystallized fraction X with the modified JMAK equation.**Figure 8.** Mean grain size versus the annealing time of the annealed AZ31 alloy.

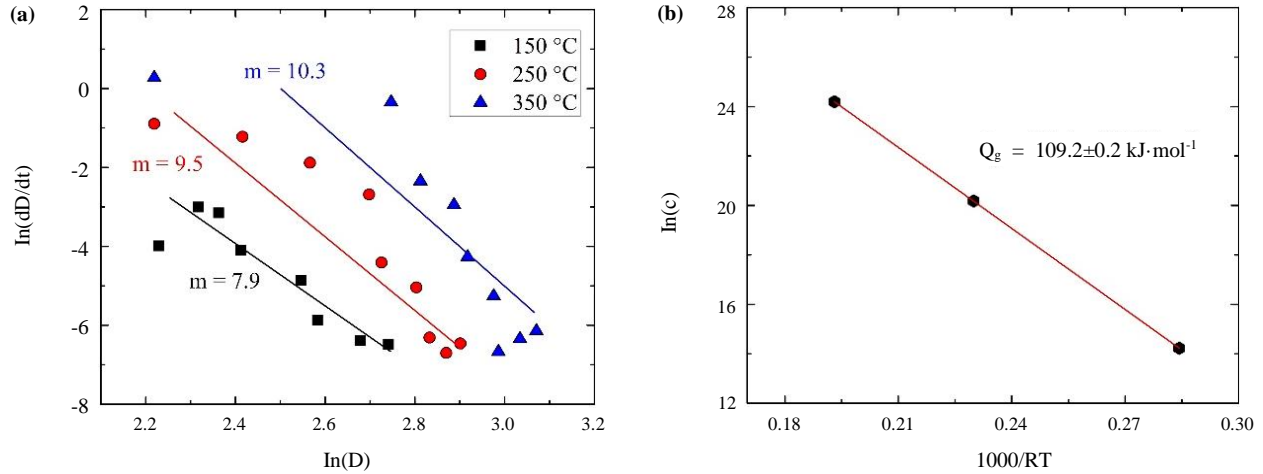


Figure 9. Plot of (a) $\ln(dD/dt)$ against $\ln D$ and (b) $\ln(c)$ as a function of $1000/RT$ of the annealed AZ31 alloy.

The high m and Q_g values may indicate a good thermal stability of the AZ31 alloy under the present deformation and annealing conditions. For comparison, Table 4 presents the grain growth activation energy reported in the literature of some AZ31 alloys and other Mg-based alloys under different deformation conditions [20,22,23,27, 30,31,36,59,60,63-65]. As shown, the reported investigations have found close range of the grain growth activation energy, except for the AZ31 and Mg-1.43Nd (wt%) alloys under severe deformation [23,36]. However, it must be noted that the m values used in these investigations were a priori fixed ($m = 2$) and not experimentally calculated.

In the present case, the m value increased with increasing annealing temperature. It can be supposed that at low annealing temperature the dislocation annihilation controlled the softening

process while at high annealing temperature the grain growth is the dominant mechanism [66].

It must be pointed out that the measured m differ from the ideal value ($m = 2$). Similar to the Avrami exponent, the grain growth exponent m is rarely found in its ideal values in the case of real experimental conditions [18,20,30,57-63]. This discrepancy is attributed to two main features: 1) the boundary mobility is very sensitive and changes with the boundary velocity and 2) the existence of a limited grain size value where the grain growth is prevented [33]. These two features are mostly related to many factors such as dislocation substructure, crystallographic texture, solute drag, and microstructure heterogeneities [29,33].

Table 4. Grain growth kinetics of some Mg-based alloys collected from the literature.

Alloy	Initial conditions		Annealing conditions		Grain growth kinetics		Ref.
	Deformation type	D_0 (μm)	T ($^{\circ}\text{C}$)	t (min)	m	Q_g ($\text{kJ}\cdot\text{mol}^{-1}$)	
AZ31	hot-rolling	9.2	150-350	5-1440	7.9-10.3	109.2	Present study
AZ31	hot-rolling	5	250-450	15-120	4	80.8	[59]
AZ31	hot-pressing	0.04	300-400	30-60	5	110	[60]
AZ31	Rolling	5.3	260-450	15-10080	5	115	[20]
AZ31	accumulate compression bonding	<1	350-450	10-240	5	105	[64]
AZ31	equal channel angular pressing	1.9	150-500	30-300	2	29 (<250 $^{\circ}\text{C}$) 92 (>250 $^{\circ}\text{C}$)	[36]
Mg-Al-Zn-Mn-Ca	hot-rolling	-	300-400	60-600	1.9-2.2	115.48	[27]
Mg-1.43Nd	high-pressure torsion	0.6	150-450	60	2	26 (<250 $^{\circ}\text{C}$) 147 (>250 $^{\circ}\text{C}$)	[23]
Mg-xSc x = 0.2, 0.3, 0.45 (wt%)	hot-rolling	-	350-450	60	3	76 (x = 0.2) 68 (x = 0.3) 100 (x = 0.45)	[31]
Mg-5Al-xTi x = 0, 10.3 (wt%)	synthesized by mechanical alloying	0.015 (x = 0) 0.022 (x = 10.3)	300-500	15-480	7 (x = 0) 8 (x = 10.3)	119 (x=0) 123 (x=10.3)	[30]
Pure Mg	hot-rolling	16.3	150-450	1-1440	13	95	[63]
Mg-3Gd-1Zn	hot-rolling	14	200-500	15-240	2.19-2.51	101	[22]
Mg-1.5Zn-0.6Zr-xEr x = 0, 0.5, 1, 2, 4 (wt%)	hot-extrusion	8 (x = 0) 3 (x = 0.5) 2.5 (x = 1) 3.3 (x = 2) 3.6 (x = 4)	250-400	90	-	23.8 (x = 0) 31.2 (x = 0.5) 34.7 (x = 1) 93.5 (x = 2) 76.2 (x = 4)	[65]

Among these, it is believed that solute drag, texture, and microstructural heterogeneity are the main factors responsible for the activation energy of the present alloy. The activation energy for grain growth was found higher than for pure Mg ($95 \text{ kJ}\cdot\text{mol}^{-1}$) [63]. In the present case, the segregation of solute atoms and impurities in grain boundaries could cause the decrease of grain boundary motion and hence the delay of grain growth. The effect of increasing the solute element concentration on the retardation of grain growth kinetics was clearly demonstrated in the Mg-xSc ($x = 0.2, 0.3, 0.45 \text{ (wt\%)}$) [31] and Mg-5Al-xTi ($x = 0, 10.3 \text{ (wt\%)}$) [30] alloys (see Table 4).

In addition, the evolution of the texture shown in Figures 10 and Figure 11 demonstrated that the hot-rolled AZ31 exhibits a typical basal texture where $\{0002\} // \text{RD-TD}$ plane [67].

It was reported earlier that the as-received (before hot-rolling) AZ31 alloy already developed a strong basal texture [34]. Consequently, the initial texture is retained after hot-rolling and then after the different annealing conditions as shown in Figure 10. However, it seems accompanied by a texture weakening as demonstrated by the evolution of texture strength index shown in Figure 12. The texture index was estimated using the MTEX toolbox [68].

The weakening of the annealing texture can be recognized by the low fraction of DRX during hot-rolling (only 10%) and the

recrystallization at shear bands that led to the formation of a variety of orientations as described in several Mg-based alloys [69-71].

The evolution of texture controls the grain boundary distribution, mobility and energy, consequently the grain growth rate. Figure 13 presents the distribution of the grain boundary misorientation of the deformed and annealed AZ31 samples. The distribution of grain boundary misorientation for random textured materials with HCP structure is superposed for comparison [72].

As evidence, neither the hot-rolled nor the annealed samples exhibit a random distribution. The hot-rolled contains about $\sim 53\%$ of sub-grain boundaries and low grain boundaries (misorientation less than 5°) resulting from the generation of dislocations due to the deformation process. Annealing at different temperatures causes the decrease of such grain boundaries owing to the development of new grains and a shift towards high misorientation (HAGBs) as noticed from the plots. However, a quite large fraction of sub-grain boundaries is still present even after the annealing of 24 h (30% at 150°C , 26% at 250°C , and 9% at 350°C , respectively). The mobility of very low angle sub-grain boundaries is reported to be governed by bulk diffusion while the grain boundary diffusion in pure metals is responsible for the mobility of high angle boundaries [73]. This may elucidate the intermediate activation energy found in the present work.

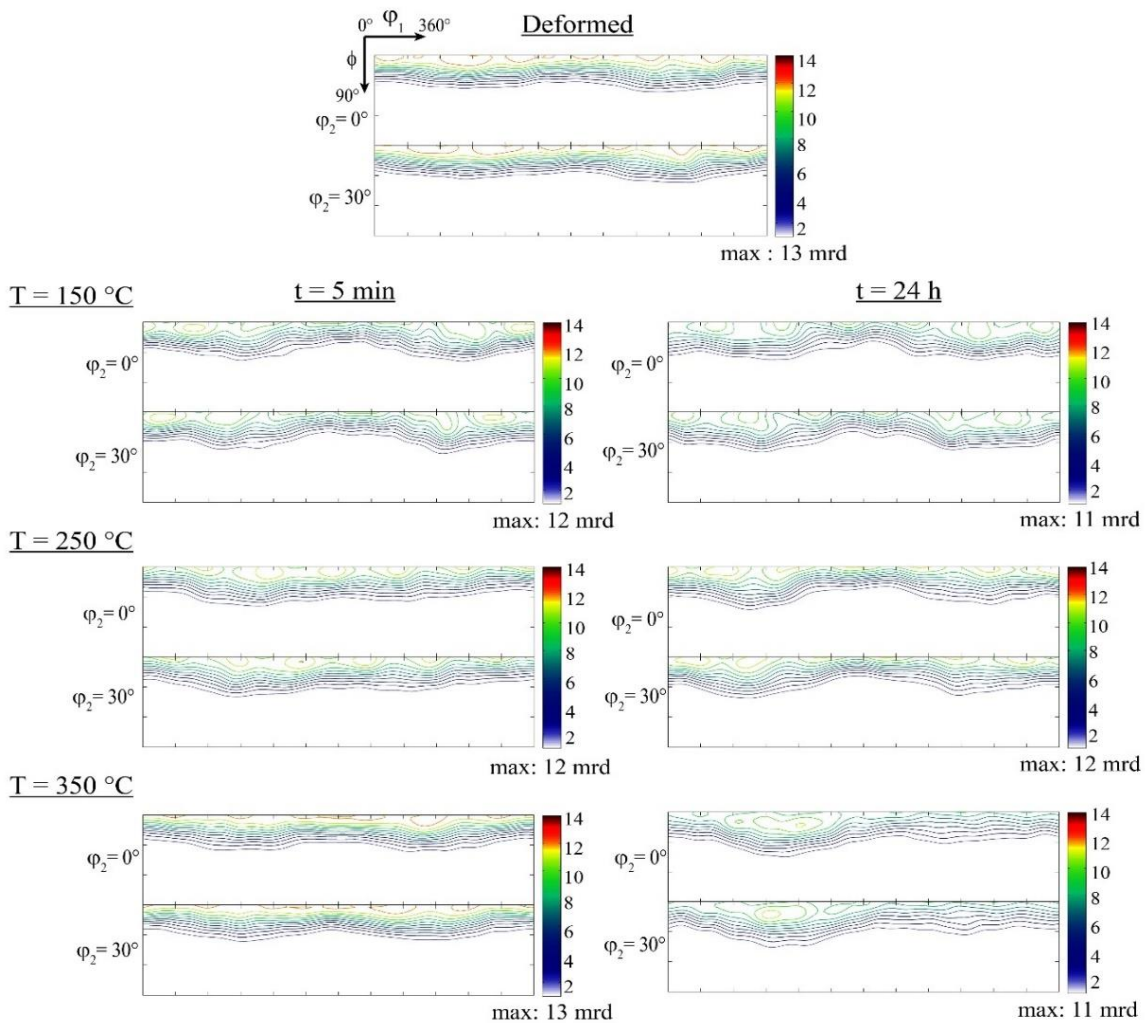


Figure 10. ODF sections at $\phi_2 = 0$ and 30° of the AZ31 alloy under deformation and different annealing conditions.

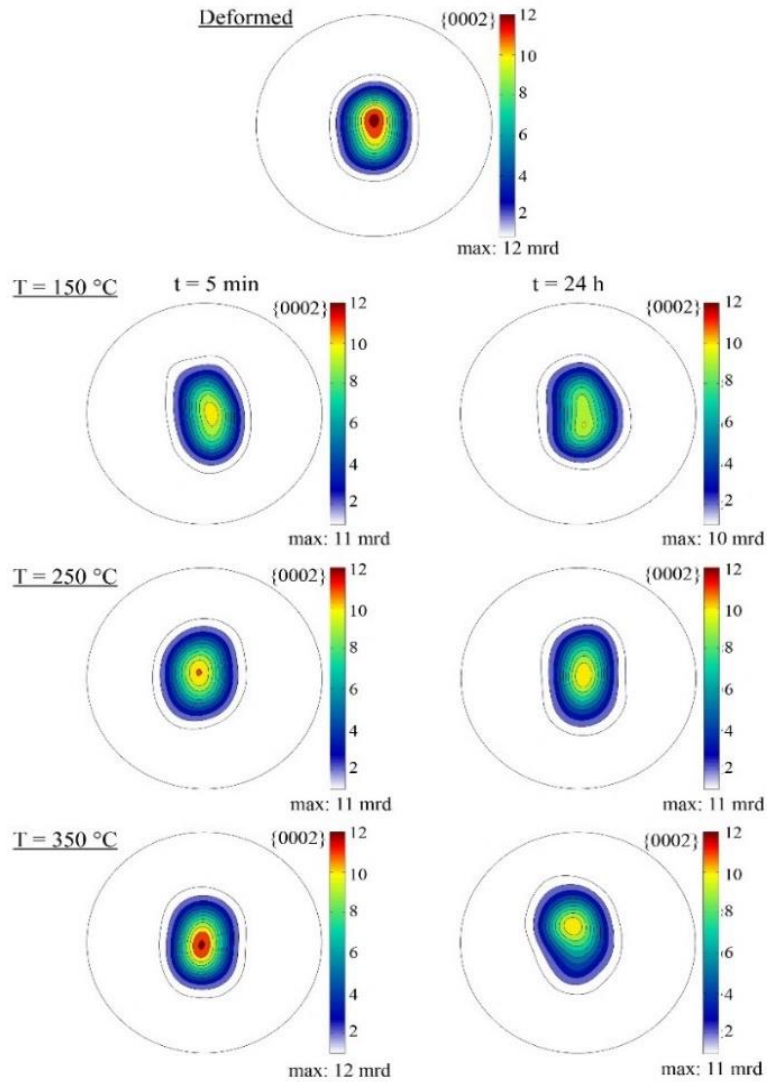


Figure 11. Recalculated {0002} pole figures of the AZ31 alloy under deformation and different annealing conditions.

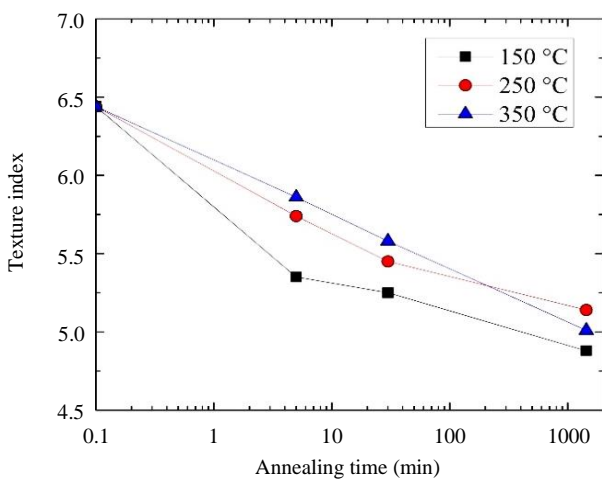


Figure 12. Evolution of texture index against annealing time.

A peak around 30° can be clearly distinguished in the annealed samples corresponding to 30° <0001> grain boundaries which resulted from the development of the basal texture [74]. Another noticeable

peak around 86° is present in the annealed samples especially after annealing at 150°C and 250°C for 5 min. This peak indicates the presence of extension twin in which the <0001> axis of the grains is reoriented by 86.8°. The presence of twins in the annealed samples means that the microstructure is still heterogeneous. To identify the different twin types and their evolution with annealing time, Figure 14 presents the IQ maps showing the different twins highlighted as extension twins (86°<11 $\bar{2}$ 0> in green), contraction twins (56°<11 $\bar{2}$ 0> in red) and double twins (38°<11 $\bar{2}$ 0> in blue) and 22°<11 $\bar{2}$ 0> (in yellow) of the annealed sample at 250°C for different durations. The fraction of different twins of the hot-rolled and annealed samples is also presented in Figure 14(d). As can be noticed, the amount of contraction 56°<11 $\bar{2}$ 0> and double 38°<11 $\bar{2}$ 0> twins decrease drastically through increasing time while the amount the 22°<11 $\bar{2}$ 0> double twin remains stable along with the entire annealing treatment. It has recently been demonstrated that Al and Zn solute elements can segregate during annealing into the twin boundaries leading to a pinning effect and hence preventing the twins from any growth [75,76]. In contrast, the fraction of extension twins 86°<11 $\bar{2}$ 0> continuously increases with increasing annealing time.

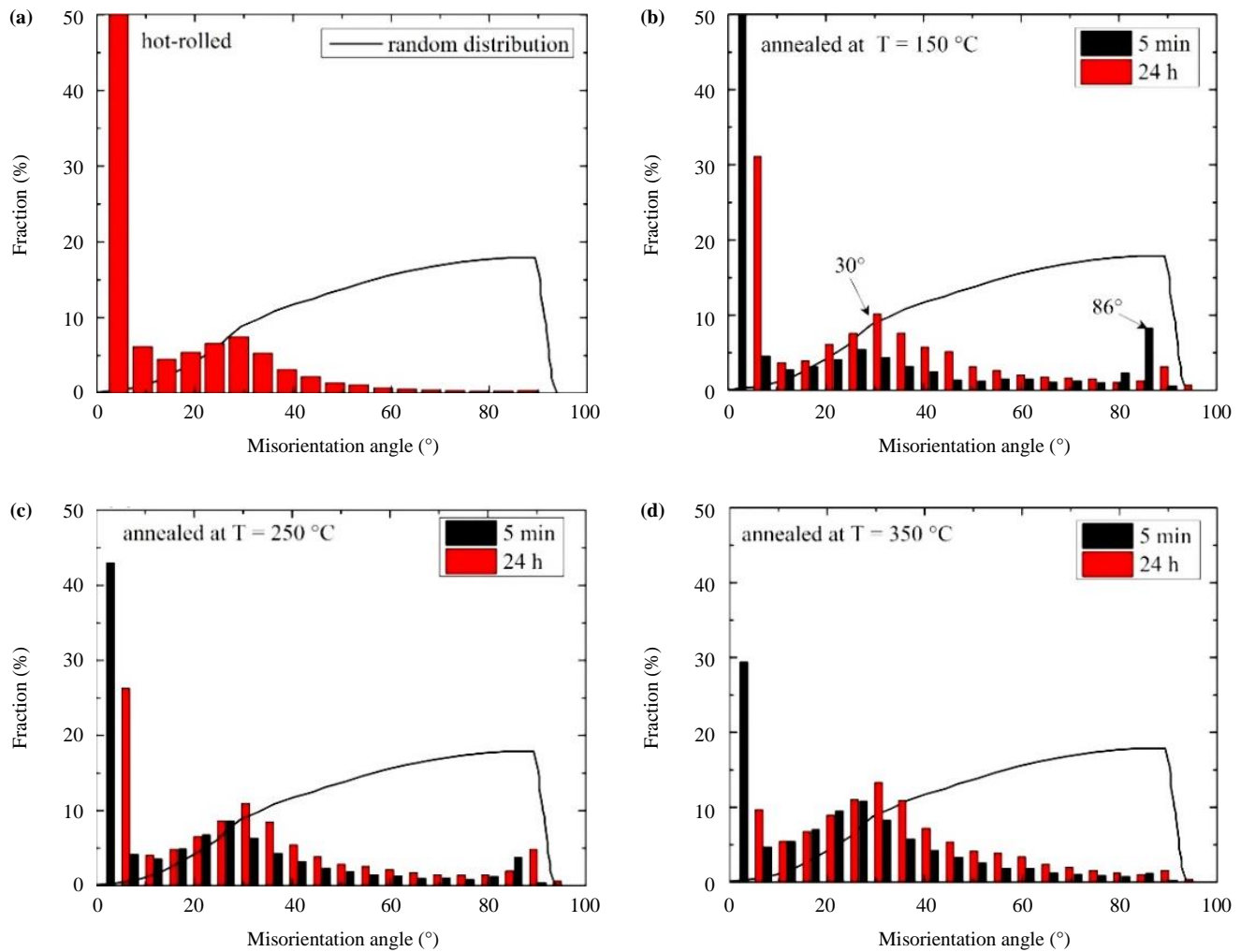


Figure 13. Grain boundary misorientation distribution of AZ31 samples: (a) hot rolled and annealed for 5 min and 24 h at (b) 150°C, (c) 250°C, and (d) 350°C.

An interesting finding (Figure 14(e)) is shown in the zoomed area of the yellow box in the IQ map of annealed sample for 30 min (Figure 14(b)). Inside the grain, a trace of twin (see the black arrows) can be noticed in which the specific twin seems to disappear or become narrower during the annealing. The present phenomenon is analog to the manifestation of the de-twinning process observed under reverse loading or unloading of twinned AZ31 alloy [76,77]. The KAM map of this zone shows high stored energy (high GND dislocation density) along the twin trace (indicated by arrows). Such observation demonstrated that twins are a source of heterogeneity in the microstructure during annealing treatment.

3.4 Hall–Petch relationship

The microhardness (Figure 2) and mean grain size values (Figure 8) were used to evaluate the static recrystallization/grain growth kinetics. Ultimately, it is interesting to check the validity of the Hall–Petch formula for the present AZ31 samples. Practically, the Hall–Petch formula can be articulated in terms of the Vickers microhardness by setting the flow stress σ equal to $H_v/3$ and this allows an indirect and very simple verification of the Hall–Petch equation [78].

For this purpose, the microhardness values were replotted versus the grain size values (Figure 15) following the Equation [78].

$$H_v = H_{v0} + \frac{K_H}{\sqrt{D}} \quad (10)$$

where H_{v0} is the friction microhardness that characterizes the lattice resistance to the motion of dislocations and K_H a parameter that reflects the role of the grain boundaries to the hardening. The H_{v0} and K_H can be estimated from a linear fitting of Equation 10. Accordingly, Figure 15 shows that the Hall–Petch relationship more or less holds over the different annealing conditions with the fitting parameters: $H_{v0} = 35.4 \pm 2.0 \text{ H}_v \cdot \mu\text{m}^{-1/2}$ and $K_H = 113.2 \pm 7.5 \text{ H}_v \cdot \mu\text{m}^{-1/2}$.

The K_H value is near to that described for other AZ31 alloys processed by rolling ($\sim 66.6 \text{ H}_v \cdot \mu\text{m}^{-1/2}$ to $145 \text{ H}_v \cdot \mu\text{m}^{-1/2}$) [79–81]. Globally, Figure 15 shows the validation of the Hall–Petch expression, however, it seems that the values at annealing for 150°C (indicated by arrow) slightly deviated compared to those at annealing for 250°C and 350°C (dash line). It can be assumed that grain size and dislocation density simultaneously participate to the hardening during annealing at low temperature (150°C). While only grain size affects the hardening at high annealing temperatures (250°C and 350°C).

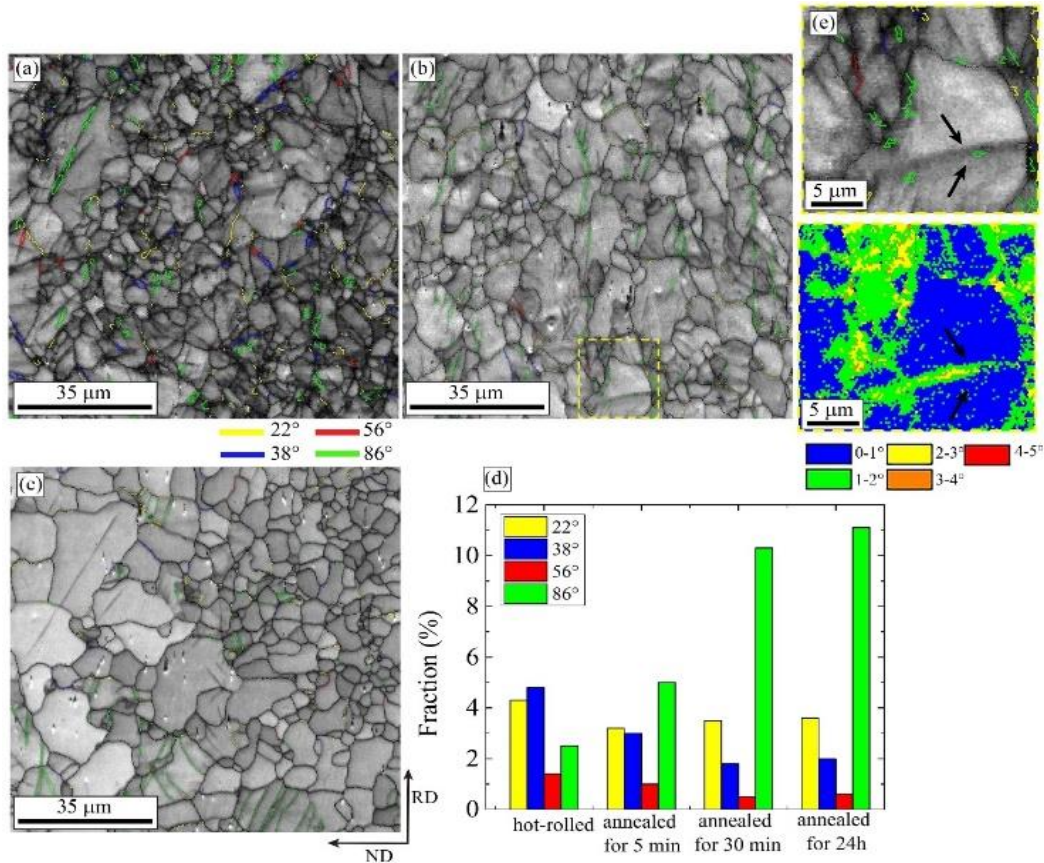


Figure 14. IQ maps highlighted with different twin types of the annealed AZ31 alloy at 250°C for: (a) 5 min, (b) 30 min, (c) 24 h, (d) fraction evolution of different twin types, and (e) IQ and KAM maps of a zoom of the yellow box, respectively.

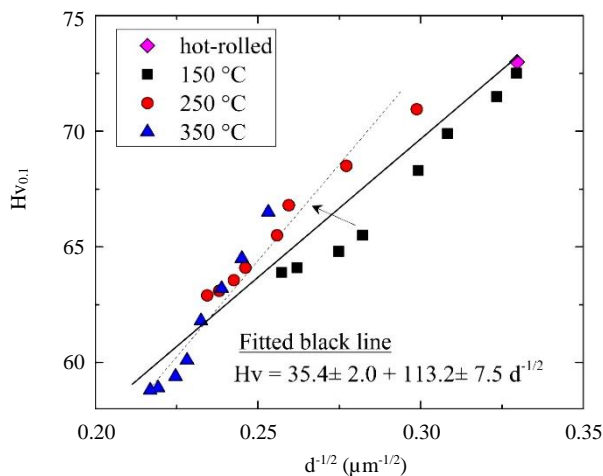


Figure 15. Microhardness replotted versus the grain size values.

4. Conclusions

- The static recrystallization/grain growth kinetics of the hot-deformed AZ31 alloy were evaluated after annealing treatments at 150°C, 250°C, and 350°C from 5 min to 24 h, respectively.
- The static recrystallization was characterized using the JMAK model and seems to occur in two regimes with two Avrami exponents and activation energies. In regime I, the Avrami exponent was found as $n = 1.5\text{-}0.35$ depending on the annealing temperature and recrystallization

activation energy of $74.1 \pm 5.7 \text{ kJ}\cdot\text{mol}^{-1}$. In regime II, a similar value of Avrami exponent was found near 0.1 to 0.2 in all annealing conditions and a very low recrystallization activation energy of $14.8 \pm 0.7 \text{ kJ}\cdot\text{mol}^{-1}$ was estimated.

- The present experimental data were in complete agreement with the modified JMAK equation: $X = A\{1 - \exp(-k_1 t^{n_1})\} + (1 - A)\{1 - \exp(-k_2 t^{n_2})\}$.
- The grain growth kinetics were well fitted by the classical equation $D^m - D_0^m = ct$ where $m = 7.9, 9.5$ and 10.3 at the temperature of 150°C, 250°C, and 350°C, respectively and the activation energy of grain growth was found to be $109 \pm 0.2 \text{ kJ}\cdot\text{mol}^{-1}$.
- Solute drag, formation of basal texture, and microstructural heterogeneities like shear bands and twinning are the main factors responsible for the recrystallization/grain growth activation energies and n and m exponent parameters of the present AZ31 alloy.
- The evolution of microhardness against the mean grain size under different annealing conditions was found to obey the Hall-Petch relationship with the fitting parameters $H_{v0} = 35.4 \pm 2.0 \text{ H}_v\cdot\mu\text{m}^{-1/2}$ and $K_H = 113.2 \pm 7.5 \text{ H}_v\cdot\mu\text{m}^{-1/2}$. Nevertheless, the dislocation density seems to contribute to the hardening at low annealing temperature (150°C).

Acknowledgements

Dr-Ing. N. Hort and Dr. D. Letzig from Magnesium Innovations Center (MagIC), Germany, are gratefully acknowledged for providing the AZ31 alloy sheet.

References

- [1] K. U. Kainer, Challenges for Implementation of Magnesium into More Applications, in: *Magnesium Technology 2016*, A. Singh, K. Solanki, M. V. Manuel, N. R. Neelameggham (Eds.), Springer International Publishing, Cham, 2016, pp. 5-6
- [2] J. Song, J. She, D. Chen, and F. Pan, "Latest research advances on magnesium and magnesium alloys worldwide," *Journal of Magnesium and Alloys*, vol. 8, pp. 1-41, 2020.
- [3] B. L. Mordike, T. Ebert, "Magnesium: Properties — applications — potential," *Materials Science and Engineering A*, vol. 302, pp. 37-45, 2001.
- [4] L. Zhang, Z. Liu, and P.-l. Mao, "Effect of annealing on the microstructure and mechanical properties of Mg-2.5Zn-0.5Y alloy," *International Journal of Minerals, Metallurgy and Materials*, vol. 21, pp. 779-784, 2014.
- [5] S. Amani, and G. Faraji, "Recrystallization and mechanical properties of WE43 magnesium alloy processed via cyclic expansion extrusion," *International Journal of Minerals, Metallurgy and Materials*, vol. 25, pp. 672-681, 2018.
- [6] F. Guo, R. Pei, L. Jiang, D. Zhang, S. Korte-Kerzel, and T. Al-Samman, "The role of recrystallization and grain growth in optimizing the sheet texture of magnesium alloys with calcium addition during annealing," *Journal of Magnesium and Alloys*, vol. 8, pp. 252-268, 2020.
- [7] F. Samadpour, G. Faraji, and A. Siahparani, "Processing of AM60 magnesium alloy by hydrostatic cyclic expansion extrusion at elevated temperature as a new severe plastic deformation method," *International Journal of Minerals, Metallurgy and Materials*, vol. 27, pp. 669-677, 2020.
- [8] Z. Zhang, J.-h. Zhang, J. Wang, Z.-h. Li, J.-s. Xie, S.-j. Liu, K. Guan, and R.-z. Wu, "Toward the development of Mg alloys with simultaneously improved strength and ductility by refining grain size via the deformation process," *International Journal of Minerals, Metallurgy and Materials*, vol. 28, pp. 30-45, 2021.
- [9] A. G. Beer, and M. R. Barnett, "Microstructure evolution in hot worked and annealed magnesium alloy AZ31," *Materials Science and Engineering A*, vol. 485, pp. 318-324, 2008.
- [10] F. Abouhilou, A. Hanna, H. Azzeddine, and D. Bradai, "Microstructure and texture evolution of AZ31 Mg alloy after uniaxial compression and annealing," *Journal of Magnesium and Alloys*, vol. 7, pp. 124-133, 2019.
- [11] A. Hanna, H. Azzeddine, R. Lachhab, T. Baudin, A.-L. Helbert, F. Brisset, Y. Huang, D. Bradai, and T. G. Langdon, "Evaluating the textural and mechanical properties of an Mg-Dy alloy processed by high-pressure torsion," *Journal of Alloys and Compounds*, vol. 778, pp. 61-71, 2019.
- [12] F. Guerza-Soualah, A. Hanna, H. Azzeddine, A.-L. Helbert, F. Brisset, T. Baudin, and D. Bradai, "The deformation and recrystallization behaviour of an Mg-Dy alloy processed by plane strain compression," *Materials Today Communications*, vol. 24, pp. 101239, 2020.
- [13] F. Guerza-Soualah, H. Azzeddine, T. Baudin, A.-L. Helbert, F. Brisset, and D. Bradai, "Microstructural and textural investigation of an Mg-Dy alloy after hot plane strain compression," *Journal of Magnesium and Alloys*, vol. 8, pp. 1198-1207, 2020.
- [14] Y. Gui, L. Ouyang, Y. Cui, H. Bian, and Q. Li, A. Chiba, "Grain refinement and weak-textured structures based on the dynamic recrystallization of Mg-9.80Gd-3.78Y-1.12Sm-0.48Zr alloy," *Journal of Magnesium and Alloys*, vol. 9, pp. 456-466, 2021.
- [15] S. Sadi, A. Hanna, H. Azzeddine, C. Casas, T. Baudin, A.-L. Helbert, F. Brisset, and J. M. Cabrera, "Characterization of microstructure and texture of binary Mg-Ce alloy processed by equal channel angular pressing," *Materials Characterization*, vol. 181, pp. 111454, 2021.
- [16] M. Kavyani, G. R. Ebrahimi, H. R. Ezatpour, and M. Jahazi, "Microstructure refinement, mechanical and biocorrosion properties of Mg-Zn-Ca-Mn alloy improved by a new severe plastic deformation process," *Journal of Magnesium and Alloys*, vol. xx, pp. xx, 2021.
- [17] R. W. Armstrong, "Engineering science aspects of the Hall-Petch relation," *Acta Mechanica*, vol. 225, pp. 1013-1028, 2014.
- [18] C. W. Su, L. Lu, and M.O. Lai, "Recrystallization and grain growth of deformed magnesium alloy," *Philosophical Magazine*, vol. 88, pp. 181-200, 2008.
- [19] H. Y. Chao, H. F. Sun, W. Z. Chen, and E. D. Wang, "Static recrystallization kinetics of a heavily cold drawn AZ31 magnesium alloy under annealing treatment," *Materials Characterization*, vol. 62, pp. 312-320, 2011.
- [20] J. J. Bhattacharyya, S. R. Agnew, and G. Muralidharan, "Texture enhancement during grain growth of magnesium alloy AZ31B," *Acta Materialia*, vol. 86, pp. 80-94, 2015.
- [21] J. Su, M. Sanjari, A. S. H. Kabir, J. J. Jonas, and S. Yue, "Static recrystallization behavior of magnesium AZ31 alloy subjected to high speed rolling," *Materials Science and Engineering A*, vol. 662, pp. 412-425, 2016.
- [22] M. Roostaei, M. Shirdel, M. H. Parsa, R. Mahmudi, and H. Mirzadeh, "Microstructural evolution and grain growth kinetics of GZ31 magnesium alloy," *Materials Characterization*, vol. 118, pp. 584-592, 2016.
- [23] S. Tighiouaret, R. Lachhab, A. Hanna, H. Azzeddine, Y. Huang, T. Baudin, A.-L. Helbert, F. Brisset, D. Bradai, and T. G. Langdon, "Thermal Stability of an Mg-Nd Alloy Processed by High-Pressure Torsion," *Advanced Engineering Materials*, vol. 21, pp. 1900801, 2019.
- [24] H. J. Frost, and M. F. Ashby, *Deformation-mechanism maps*, Pergamon Press, Oxford, 1982.
- [25] A. D. Murphy, and J. E. Allison, "The Recrystallization Behavior of Unalloyed Mg and a Mg-Al Alloy," *Metallurgical and Materials Transactions A*, vol. 49, pp. 1492-1508, 2018.
- [26] H. Zhao, P.-j. Li, and L.-j. He, "Kinetics of recrystallization for twin-roll casting AZ31 magnesium alloy during homogenization," *International Journal of Minerals, Metallurgy and Materials*, vol. 18, pp. 570, 2011.
- [27] Q. Wang, B. Jiang, A. Tang, J. Fu, Z. Jiang, H. Sheng, D. Zhang, G. Huang, and F. Pan, "Unveiling annealing texture formation and static recrystallization kinetics of hot-rolled Mg-Al-Zn-Mn-Ca alloy," *Journal of Materials Science and Technology*, vol. 43, pp. 104-118, 2020.

- [28] J.-W. Park, H.-J. Jeong, S.-W. Jin, M.-J. Kim, K. Lee, J. J. Kim, S.-T. Hong, and H.N. Han, "Effect of electric current on recrystallization kinetics in interstitial free steel and AZ31 magnesium alloy," *Materials Characterization*, vol. 133, pp. 70-76, 2017.
- [29] G. T. Higgins, "Grain-Boundary Migration and Grain Growth," *Metal Science*, vol. 8, pp. 143-150, 1974.
- [30] M. A. Thein, L. Lu, and M. O. Lai, "Kinetics of grain growth in nanocrystalline magnesium-based metal-metal composite synthesized by mechanical alloying," *Composites Science and Technology*, vol. 66, pp. 531-537, 2006.
- [31] C. J. Silva, A. Kula, R. K. Mishra, and M. Niewczas, "Grain growth kinetics and annealed texture characteristics of Mg-Sc binary alloys," *Journal of Alloys and Compounds*, vol. 687, pp. 548-561, 2016.
- [32] Z. Jin, D. Yu, X. Wu, K. Yin, and K. Yan, "Drag Effects of Solute and Second Phase Distributions on the Grain Growth Kinetics of Pre-Extruded Mg-6Zn Alloy," *Journal of Materials Science and Technology*, vol. 32, pp. 1260-1266, 2016.
- [33] J. Humphreys, G. S. Rohrer, and A. Rollett, Chapter 7 - Recrystallization of Single-Phase Alloys, in: *Recrystallization and Related Annealing Phenomena (Third Edition)*, J. Humphreys, G. S. Rohrer, A. Rollett (Eds.), Elsevier, Oxford, 2017, pp. 245-304
- [34] S. Tighiouaret, A. Hanna, H. Azzeddine, L. Rabahi, A. Dakhouche, F. Brisset, A.-L. Helbert, T. Baudin, and D. Bradai, "On the evolution of microstructure, texture and corrosion behavior of a hot-rolled and annealed AZ31 alloy," *Materials Chemistry and Physics*, vol. 267, pp. 124598, 2021.
- [35] J. Su, and S. Yue, "Texture Weakening and Grain Refinement by High Speed Rolling and Annealing of an AZ31 Magnesium Alloy, in: K.N. Solanki, D. Orlov, A. Singh, N.R. Neelameggham (Eds.) Magnesium Technology 2017, Springer International Publishing, Cham, 2017, pp. 547-554
- [36] C. W. Su, L. Lu, and M. O. Lai, "Mechanical behaviour and texture of annealed AZ31 Mg alloy deformed by ECAP," *Materials Science and Technology*, vol. 23, pp. 290-296, 2007.
- [37] H.-K. Kim, "Activation energies for the grain growth of an AZ31 Mg alloy after equal channel angular pressing," *Journal of Materials Science*, vol. 39, pp. 7107-7109, 2004.
- [38] A. Hanna, A. Dakhouche, K. Tirsatine, A. Sari, Y. Khereddine, D. Bradai, and H. Azzeddine, "Effect of hot rolling on the corrosion behavior of AZ31 magnesium alloy," *Metallurgical Research and Technology*, vol. 116, pp. 109, 2019.
- [39] Y. Mikami, K. Oda, M. Kamaya, and M. Mochizuki, "Effect of reference point selection on microscopic stress measurement using EBSD," *Materials Science and Engineering A*, vol. 647, pp. 256-264, 2015.
- [40] R. Hielscher, and H. Schaeben, "A novel pole figure inversion method: specification of the MTEX algorithm," *Journal of Applied Crystallography*, vol. 41, pp. 1024-1037, 2008.
- [41] J.-H. Cho, A. D. Rollett, and K. H. Oh, "Determination of a mean orientation in electron backscatter diffraction measurements," *Metallurgical and Materials Transactions A*, vol. 36, pp. 3427-3438, 2005.
- [42] K. Atik, and M. Efe, "Twinning-induced shear banding and its control in rolling of magnesium," *Materials Science and Engineering A*, vol. 725, pp. 267-273, 2018.
- [43] Y. Wang, Y. Xin, H. Yu, L. Lv, and Q. Liu, "Formation and microstructure of shear bands during hot rolling of a Mg-6Zn-0.5Zr alloy plate with a basal texture," *Journal of Alloys and Compounds*, vol. 644, pp. 147-154, 2015.
- [44] M. Avrami, "Kinetics of phase change. i general theory," vol. 7, pp. 1103-1112, 1939.
- [45] J. W. Christian, *The Theory of Transformations in Metals and Alloys: Advanced Textbook in Physical Metallurgy*, Peramon Press, Oxford, 1975.
- [46] P. N. Kalu, and D. R. Waryoba, "A JMAK-microhardness model for quantifying the kinetics of restoration mechanisms in inhomogeneous microstructure," *Materials Science and Engineering A*, vol. 464, pp. 68-75, 2007.
- [47] M. Oyarzábal, A. Martínez-de-Guerenu, and I. Gutiérrez, "Effect of stored energy and recovery on the overall recrystallization kinetics of a cold rolled low carbon steel," *Materials Science and Engineering A*, vol. 485, pp. 200-209, 2008.
- [48] A. D. Rollett, D. J. Srolovitz, R. D. Doherty, and M. P. Anderson, "Computer simulation of recrystallization in non-uniformly deformed metals," *Acta Metallurgica*, vol. 37, pp. 627-639, 1989.
- [49] W. Pantleon, "Resolving the geometrically necessary dislocation content by conventional electron backscattering diffraction," *Scripta Materialia*, vol. 58, pp. 994-997, 2008.
- [50] R. Badji, T. Chauveau, and B. Bacroix, "Texture, misorientation and mechanical anisotropy in a deformed dual phase stainless steel weld joint," *Materials Science and Engineering A*, vol. 575, pp. 94-103, 2013.
- [51] Y. I. Bourezg, D. Elfiad, H. Azzeddine, and D. Bradai, "Investigation of recrystallization kinetics in hot-rolled Mg-La alloy using differential scanning calorimetry technique," *Thermochimica Acta*, vol. 690, pp. 178688, 2020.
- [52] T. Zhang, L. Li, S. Lu, Z. Li, P. Chen, H.J.M.R.T. Gong, "Static recrystallization kinetics and microstructure evolution of 7055 aluminum alloy," vol. 116, pp. 120, 2019.
- [53] E. A. Jäggle, and E. J. Mittemeijer, "The Kinetics of and the Microstructure Induced by the Recrystallization of Copper," *Metallurgical and Materials Transactions A*, vol. 43, pp. 1117-1131, 2012.
- [54] A. Morozova, A. Dolzhenko, M. Odnobokova, A. P. Zhilyaev, A. Belyakov, and R. Kaibyshev, "Annealing Behavior and Kinetics of Primary Recrystallization of Copper," *Defect and Diffusion Forum*, vol. 385, pp. 343-348, 2018.
- [55] T. Matsui, T. Ogawa, and Y. Adachi, "Relationship between three-dimensional microstructure and Avrami exponent for recrystallization in pure iron," *Results in Materials*, vol. 1, pp. 100002, 2019.
- [56] J. E. Burke, and D. Turnbull, "Recrystallization and grain growth," *Progress in Physics of Metals*, vol. 3, pp. 220-292, 1952.
- [57] S. Abdessameud, H. Azzeddine, B. Alili, and D. Bradai, "Grain growth in AZ31 alloy after uniaxial compression," *Transaction of Nonferrous Metals Society of China*, vol. 20, pp. 2215-2222, 2010.

- [58] P. Cao, L. Lu, and M. O. Lai, "Grain growth and kinetics for nanocrystalline magnesium alloy produced by mechanical alloying," *Materials Research Bulletin*, vol. 36, pp. 981-988, 2001.
- [59] Q. Miao, L. Hu, X. Wang, and E. Wang, "Grain growth kinetics of a fine-grained AZ31 magnesium alloy produced by hot rolling," *Journal of Alloys and Compounds*, vol. 493, pp. 87-90, 2010.
- [60] X. Wang, L. Hu, K. Liu, Y. Zhang, "Grain growth kinetics of bulk AZ31 magnesium alloy by hot pressing," *Journal of Alloys and Compounds*, vol. 527, pp. 193-196, 2012.
- [61] S. Abdessameud, and D. Bradai, "Microstructure and Texture evolution in hot rolled and annealed magnesium alloy TRC AZ31," *Canadian Metallurgical Quarterly*, vol. 48, pp. 433-442, 2009.
- [62] H. Azzeddine, and D. Bradai, "On the texture and grain growth in hot-deformed and annealed WE54 alloy," *International Journal of Materials Research*, vol. 103, pp. 1351-1360, 2012.
- [63] D. Panda, R. K. Sabat, S. Suwas, V. D. Hiwarkar, and S. K. Sahoo, "Texture weakening in pure magnesium during grain growth," *Philosophical Magazine*, vol. 99, pp. 1362-1385, 2019.
- [64] J. Ma, X. Yang, Q. Huo, H. Sun, J. Qin, J. Wang, "Mechanical properties and grain growth kinetics in magnesium alloy after accumulative compression bonding," *Materials & Design*, vol. 47, pp. 505-509, 2013.
- [65] J. Zhang, W. Li, Z. Guo, "Static recrystallization and grain growth during annealing of an extruded Mg-Zn-Zr-Er magnesium alloy," *Journal of Magnesium and Alloys*, vol. 1, pp. 31-38, 2013.
- [66] J. Stráská, M. Janeček, J. Čížek, J. Stráský, and B. Hadzima, "Microstructure stability of ultra-fine grained magnesium alloy AZ31 processed by extrusion and equal-channel angular pressing (EX-ECAP)," *Materials Characterization*, vol. 94, pp. 69-79, 2014.
- [67] Y. N. Wang, J. C. Huang, "Texture analysis in hexagonal materials," *Materials Chemistry and Physics*, vol. 81, pp. 11-26, 2003.
- [68] H. J. Bunge, "Texture Analysis in Materials Science: Mathematical Methods", 1st ed., Butterworth-Heinemann Ltd, 1982.
- [69] I. Basu, T. Al-Samman, and G. Gottstein, "Shear band-related recrystallization and grain growth in two rolled magnesium-rare earth alloys," *Materials Science and Engineering A*, vol. 579, pp. 50-56, 2013.
- [70] M. R. Barnett, M. D. Nave, and C. J. Bettles, "Deformation microstructures and textures of some cold rolled Mg alloys," *Materials Science and Engineering A*, vol. 386, pp. 205-211, 2004.
- [71] J. Bohlen, M. R. Nürnberg, J. W. Senn, D. Letzig, and S. R. Agnew, "The texture and anisotropy of magnesium-zinc-rare earth alloy sheets," *Acta Materialia*, vol. 55, pp. 2101-2112, 2007.
- [72] A. Morawiec, "Misorientation-Angle Distribution of Randomly Oriented Symmetric Objects," *Journal of Applied Crystallography*, vol. 28, pp. 289-293, 1995.
- [73] F. J. Humphreys, and M. Hatherly, Chapter 8 - Recrystallization of Ordered Materials, in: *Recrystallization and Related Annealing Phenomena (2nd Edition)*, F.J. Humphreys, M. Hatherly (Eds.), Elsevier, Oxford, 2004, pp. 269-283
- [74] J. Valle, M. Pérez-Prado, and O. J. R. D. M. Ruano, "The distribution of disorientation angles in a rolled AZ31 Mg alloy," *Revista de Metalurgia*, vol. 38, pp. 353-357, 2002.
- [75] Y. Cui, Y. Li, Z. Wang, X. Ding, Y. Koizumi, H. Bian, L. Lin, and A. Chiba, "Impact of solute elements on detwinning in magnesium and its alloys," *International Journal of Plastics Technology*, vol. 91, pp. 134-159, 2017.
- [76] Y. Xin, X. Zhou, H. Chen, J.-F. Nie, H. Zhang, Y. Zhang, and Q. Liu, "Annealing hardening in detwinning deformation of Mg-3Al-1Zn alloy," *Materials Science and Engineering A*, vol. 594, pp. 287-291, 2014.
- [77] Z. Keshavarz, and M. Barnett, In-situ investigation of twinning behaviour in Mg-3Al-1Zn, in: N.R. Neelameggham, H.I. Kaplan, B.R. Powell (Eds.) *Magnesium Technology Symposium (6th: 2005: San Francisco, Calif.)*, TMS, San Francisco, USA, 2005, pp. 171-175
- [78] M. Furukawa, Z. Horita, M. Nemoto, R. Z. Valiev, and T. G. Langdon, "Factors influencing the flow and hardness of materials with ultrafine grain sizes," *Philos. Mag. A*, vol. 78, pp. 203-216, 1998.
- [79] A. Jain, O. Duygulu, D. W. Brown, C. N. Tomé, and S. R. Agnew, "Grain size effects on the tensile properties and deformation mechanisms of a magnesium alloy, AZ31B, sheet," *Materials Science and Engineering A*, vol. 486, pp. 545-555, 2008.
- [80] L. Guo, Z. Chen, and L. Gao, "Effects of grain size, texture and twinning on mechanical properties and work-hardening behavior of AZ31 magnesium alloys," *Materials Science and Engineering A*, vol. 528, pp. 8537-8545, 2011.
- [81] R. L. Doiphode, S. V. S. N. Murty, N. Prabhu, and B. P. Kashyap, "Grain growth in calibre rolled Mg-3Al-1Zn alloy and its effect on hardness," *Journal of Magnesium and Alloys*, vol. 3, pp. 322-329, 2015.